Acta Geochim (2023) 42(2):256–265
https://doi.org/10.1007/s11631-022-00591-6

ORIGINAL ARTICLE

Depth profiling of arsenian pyrite in Carlin-type ores through wet chemistry

Meizhi Yang[1,2] · Quan Wan[1,3] · Xin Nie[1] · Suxing Luo[4] · Yuhong Fu[5] · Ping Zeng[1,2] · Wenqi Luo[1,2]

Received: 29 November 2022 / Revised: 18 December 2022 / Accepted: 19 December 2022 / Published online: 27 December 2022

Abstract Enrichment of As and Au at the overgrowth rims of arsenian pyrite is a distinctive feature of Carlin-type gold ores. Revealing distribution of such key elements in high resolution is of fundamental importance yet often proves challenging. In this study, repeated non-oxidative acid etching of ore samples from Shuiyindong gold deposit was applied to enable elemental depth profiling of gold-bearing arsenian pyrite grains. ICP-OES and AAS were used to determine the dissolved Fe, As, and Au concentrations in each of the etching solutions, and XPS was carried out to exam the etched mineral surfaces. In contrast to conventional ion beam etching that may cause substantial sample damage, our acid etching method does not seem to significantly alter the composition and chemical state of the samples. The etched depths directly converted from the measured elemental concentrations can reproducibly reach a very high resolution of $\sim$ 1 nm, and can be conveniently controlled through varying the etching time. While the Fe and As depth profiles consistently reflect the surface oxidation property of arsenian pyrite, the Au profile displaying an obvious upward trend reveals the ore fluid evolution at the late stage of mineralization. Based on our experimental results, we demonstrate that our wet chemistry method is capable of effective depth profiling of gold ore and perhaps other geological samples, with advantages surpassing many instrumental techniques including negligible sample damage, nanoscale resolution as well as isotropic etching.

Keywords Wet chemistry · Acid etching · Depth profiling · Carlin-type gold deposits · Arsenian pyrite

1 Introduction

Carlin-type gold deposits are of great economic significance, as exemplified by the over 800t of gold reserve in just Dian-Qian-Gui "Golden Triangle" area in Southwest China (Su et al. 2018). The major gold-bearing mineral in such deposits is arsenian pyrite, which often shows a core-rim structure with As and Au enriched in the overgrowth rims (Muntean et al. 2011; Simon et al. 1999b). High resolution techniques such as NanoSIMS have revealed heterogeneous distribution of Au and As exhibiting an oscillatory zoning feature underneath the mineral surface (Barker et al. 2009; Li et al. 2020; Yan et al. 2018). Mechanistic interpretation of compositional correlation between As and Au (in the form of either Au^{+} or Au nanoparticles) as well as the formation process of Au nanoparticles was proposed through linearly relating the solubility of Au in arsenian pyrite to the As content (Deditius et al. 2014; Reich et al. 2005), while alternative explanations on gold existing forms were also reported

✉ Quan Wan
wanquan@vip.gyig.ac.cn

[1] State Key Laboratory of Ore Deposit Geochemistry, Institute of Geochemistry, Chinese Academy of Sciences, Guiyang 550081, China

[2] University of Chinese Academy of Sciences, Beijing 100049, China

[3] CAS Center for Excellence in Comparative Planetology, Hefei 230026, China

[4] Department of Chemistry and Chemical Engineering, Zunyi Normal College, Zunyi 563006, China

[5] School of Geographic and Environmental Sciences, Guizhou Normal University, Guiyang 550001, China

(Mikhlin and Romanchenko 2007; Moller and Kersten 1994). The concentration, chemical state of elements such as Au and As, along with their spatial distributions, are all essential properties of Carlin-type gold ores, which provide crucial insights into the complex ore fluid evolution as well as the mineralization processes (Agangi et al. 2013; Barker et al. 2009; Reich et al. 2013; Zhao et al. 2018). On the other hand, comprehensive understanding of such occurrence states of ore-forming elements also helps to improve metallurgical technology for the refractory Carlin-type gold ores (Mao 1991). Therefore, discovering the occurrence states of elements in arsenian pyrite grains have always remained as an extensively studied topic (Fleet and Mumin 1997; Hu et al. 2017; Large et al. 2009; Su et al. 2012; Zheng et al. 2016).

A number of in-situ instrumental techniques were used to perform spot or area analysis of elemental contents on gold-bearing minerals, including electron probe microanalyzer (EPMA), laser ablation inductively coupled plasma mass spectrometry (LA-ICP-MS), secondary ion mass spectroscopy (SIMS), etc. (Cepedal et al. 2008; Hou et al. 2016; Li et al. 2020; Reich et al. 2005; Zhang et al. 2003; Zhao et al. 2018). To determine the compositional or structural properties as a function of depth beneath the mineral surface (i.e., depth profiling), surface etching methods typically involving energetic beams (such as ion sputtering and laser ablation) were used to remove and expose surface materials stepwise. Such physical etching techniques usually equipped with sensitive analytical instruments (as shown above) have the advantage of achieving in-situ analytical results with up to ppb level detection limits (Della et al. 2017; Dowsett and Adriaens 2004; Hnatyshin et al. 2020; Yamaguchi et al. 2020). Yet, such depth profiling methodology suffers several substantial drawbacks mainly due to the nature of high energy etching. While the depth is quantitatively converted from the etching timescale, the composition-dependent etching rate (matrix effect) prevents straightforward calibration for often unspecified geological samples (Wang et al. 2009). The potential radiation damage may change the chemical state (e.g. valence) of certain labile elements and create distortion to the elemental ratios (Brijs et al. 1993; Nobuta and Ogawa 2009). Besides, in contrast to chemical etching, physical etching is usually anisotropic with high energy beams directed at arbitrarily selected mineral surfaces, which may lead to biased analytical signals.

In this research, we developed a simple but effective wet chemical method with non-oxidizing acid to etch gold-bearing arsenian pyrite in a controlled manner. We demonstrate that depth profiling of arsenian pyrite through wet chemistry can successfully obtain the spatial distribution features of key elements with satisfactory sample representativeness. Eventually, these characterization results are expected to promote advancing the minerogenesis and metallurgy in Carlin-type gold deposits.

2 Materials and methods

2.1 Sample preparation

Ore samples used in this study were collected from Shuiyindong, a super-large Carlin-type gold deposit in Guizhou, China (Zhang et al. 2010). The grade of our ore samples was determined to be $\sim$ 220 ppm. Arsenian pyrite is the major gold-bearing mineral and the host rock is mainly composed of carbonate (Liang et al. 2013; Su et al. 2008). Since natural gold-bearing pyrite samples discussed in this paper all contain As, we do not distinguish pyrite from arsenian pyrite hereinafter. Ore samples were grouped into bulk and powder respectively, with bulk sample mechanical polished. A portion of bulk sample was crushed, milled (< 200 mesh), ultrasonicated (1 h in deionized water) and panned to collect powder sample, which was dried and stored in vacuum, and named SG-0.

To perform wet chemical etching, the initial pyrite powder sample SG-0 was soaked with 3 M HCl in an ultrasonic bath (100 W, 40 kHz) for 90 min, with the solid-to-liquid ratio maintained at 1:50. The temperature in the ultrasonic bath was found to raise from $\sim$ 20 to $\sim$ 45 °C till the end of the etching process. Subsequently, the suspension was separated by centrifugation, and the resulting aqueous solution sample was named SG-0_{aq}. The remaining solid powder sample, washed with anhydrous ethanol at least 9 times, then dried and stored in an anaerobic tank (Luo et al. 2018), was named SG-1. And the etched pyrite layer (from calculation) in the 1st acid etching turn was designated as SG-0_s. The above procedure was repeated (for up to 8 times) to obtain samples SG-N_{aq}, SG-N, and SG-N_s, respectively, with N indicating the acid etching step(s) experienced by the powder samples (SG-N).

2.2 Instrumental characterization

The Au, As, Fe and S contents and distributions in bulk ore samples were obtained by EPMA (JEOL, JXA-8230) with spot size of 1 um. The total elemental contents of pyrite powders were analyzed by X-ray fluorescence spectrometry (XRF, ARL Perform'X 4200, Thermo Fisher, USA). And the mineral composition was determined by X-ray diffraction (XRD, Empyrean, PANalytical B.V, NL) with Cu-$K\alpha$ radiation. Morphology of solid powder samples were observed by scanning electron microscopy (SEM, Scios, FEI, USA), and the ImageJ software was used to estimate the average particle size of pyrite. Fe and As concentrations in etching solutions (SG-N_{aq}) were detected

by inductively coupled plasma optical emission spectrometry (ICP-OES, VISTA-MPX, Varian, USA). To obtain the Au content, etching solutions were first digested by fresh 10% (V/V) aqua regia, then analyzed with atomic absorption spectroscopy (AAS, 990SUPER, Persee, China).

Furthermore, the chemical state and content of elements at the surface of pyrite grains from our powder samples (SG-N) were analyzed by X-ray photoelectron spectroscopy (XPS, AXIS SUPRA, Shimadzu, Japan), with Al-$K\alpha$ exciting radiation (1486.6 eV, 450 W), 300 × 700 μm analysis size, 0.05 eV step size and 500 ms dwell time, and 6–8 sweeps. All spectra were analyzed by the CasaXPS software and calibrated with the adventitious Carbon 1*s* peak at 284.8 eV. The Shirley type background subtraction was applied, and high resolution spectra were fitted with the Gaussian (30%)–Lorentz (70%) function (Artyushkova et al. 2007). Finally, the concentrations of elements on etched pyrite surfaces were roughly estimated by CasaXPS.

2.3 Concentration and depth estimations

To estimate the elemental contents in the dissolved surface layer of pyrite, we used a commonly accepted pyrite formula as $FeAs_XS_{(2-X)}$, assuming during the formation of arsenian pyrite, one sulfur atom was substituted by one arsenic atom, and neglecting all other trace elements in pyrite (Liang et al. 2013; Su et al. 2012; Wang and Zhu 2015). Thus, the atomic percentage of Au or As in the dissolved pyrite after each acid etching was calculated with the Eq. (1) below:

$$\text{As or Au (at.\%)} = \frac{N_{\text{Au}} \text{ or } N_{\text{As}}}{3N_{\text{Fe}}} \times 100\% \quad (1)$$

where N_{Au}, N_{As} and N_{Fe} denote the atomic quantity of Au, As and Fe in the dissolved pyrite respectively.

Moreover, to simplify the calculation of the thickness of the etched/dissolved pyrite layer, all pyrite particles were reasonably assumed to be cubic in shape, and the etched depth in each etching step was estimated with Eq. (2):

$$\Delta D = \frac{D\left(1 - \sqrt[3]{\frac{\Delta m}{m}}\right)}{2} \quad (2)$$

where D represents the side length of pyrite cubes, m is the total mass of pyrite in SG-N, and Δm stands for weight loss due to pyrite dissolution (the etched pyrite layer), respectively. To calculate Δm, the measured Fe and As contents in $SG\text{-}N_{aq}$, and the converted S content based on the fixed atomic ratio of Fe:(S + As) = 1:2 were added up.

3 Results and discussions

3.1 EPMA analysis of bulk sample

The Au and As contents and their distributions in arsenian pyrite are important characteristics of Carlin-type gold deposits. We first used EPMA to characterize elemental contents and distributions on the surface of the polished bulk samples. Previous researches have demonstrated the existence of overgrowth rims in arsenian pyrite grains, with Au enriched in As-rich rims (Gopon et al. 2019; Palenik et al. 2004), and the overgrowth rims generally have much higher Au concentrates than the core (Mao 1991; Zhao et al. 2018). Consistently, pyrite in this study from Shuiyindong Carlin-type gold deposit also shows such characteristics (Fig. 1), with Au in the arsenic-rich rim reaching up to 0.07 mol%. Based on EPMA elemental mapping, As may be distributed in both the core and rim of pyrite grain as shown in Fig. 1d, with the outer rim having relatively higher As, and Au being enriched in this As-rich rim. Fe distribution in the whole grain appears relatively homogeneous, whereas S is slightly poor in the rim. Meanwhile, a relatively strong negative correlation between S and As with regard to both their concentrations and spatial distributions has been observed (Fig. 1f), compatible with the well-established isomorphic substitution of S^- by As^- (Liang et al. 2013; Su et al. 2012; Wang and Zhu 2015). The occurrence of As (as As^-) was also confirmed in our XPS analysis (see Sect. 3.4).

3.2 Composition of powder samples

The Shuiyindong ore samples are known to be mainly composed of dolomite, silica, pyrite, and a small amount of clay mineral (Su et al. 2008), which is verified by XRD analysis (not shown) of our initial powder sample SG-0. The 1st round of acid treatment with HCl almost appeared to completely dissolve dolomite from SG-0, and thus significantly concentrated pyrite in SG-1. Specifically, the resulting total content of pyrite in SG-1 became 32 wt% (from XRF analysis), corresponding to ∼ 24 wt% pyrite in SG-0, with the weight lost from the first acid treatment step (∼ 42 wt% of SG-0) attributed to the acid removal of carbonate minerals. Based on SEM image analysis, the average grain size of pyrite was below 20 μm in both SG-0 and SG-1, and practically little difference in pyrite morphology and size was detected between the two samples. Furthermore, despite of stepwise mineral etching by the non-oxidative acid (HCl) of relatively high concentration (3 M), the overall compositions as well as the morphology of pyrite in samples SG-N (N = 1–7) remained nearly the same.

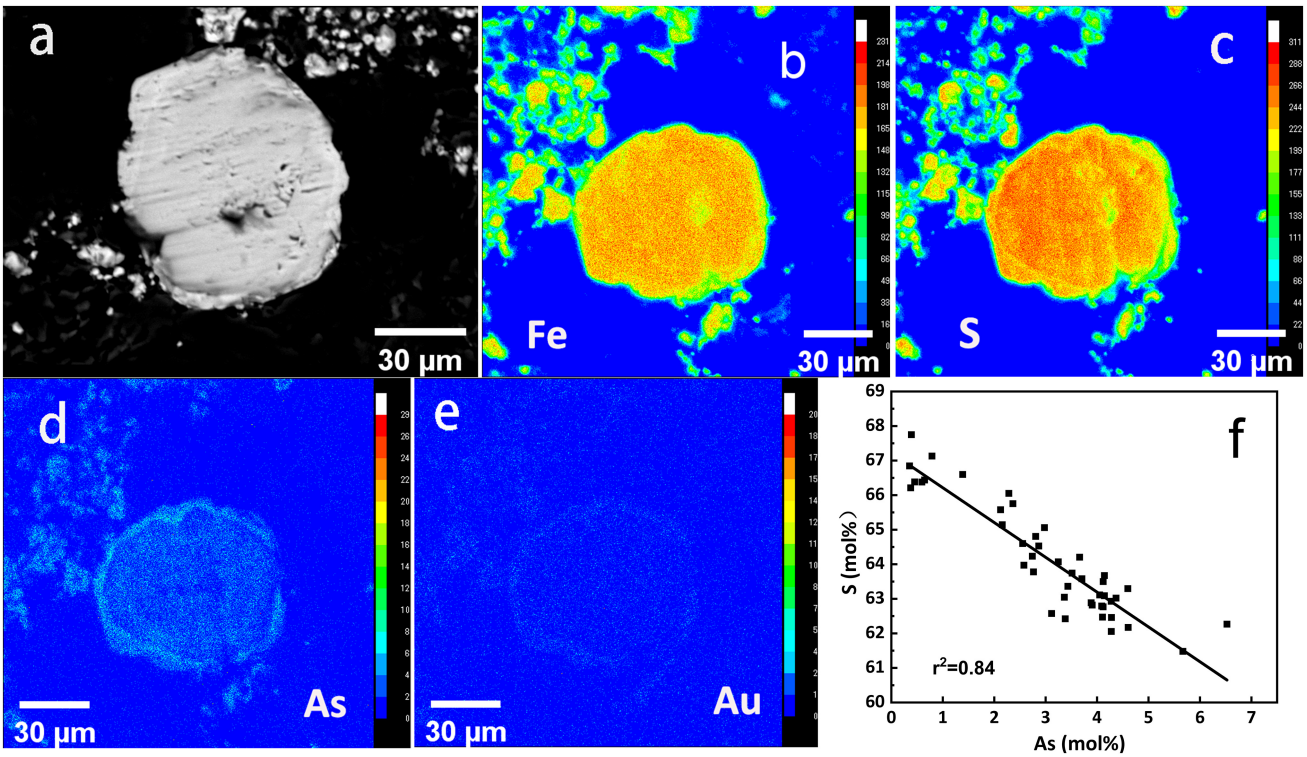

Fig. 1 Backscattered electron image of a pyrite grain (**a**), Fe (**b**), S (**c**), As (**d**) and Au (**e**) mapping by EPMA, and a negative correlation between As and S concentrations (**f**)

3.3 Acid etching of pyrite

It should be noted that Fe, S, As and Au contents detected in etching solutions are all assumed to originate from dissolution of pyrite, as supported by general knowledge of Carlin-type gold ores (Deditius et al. 2014; Simon et al. 1999a). Therefore, here we focus our discussion on acid etching of pyrite, with the Fe, As and Au concentrations data presented in Table 1 As shown in Fig. 2a–c, the overall variations of Fe, As and Au contents with each etching solution appear somewhat similar. The elemental concentrations always showed the highest values at the first acid etching step, dramatically decreased at the second step, and then became relatively steady after several repeated steps. For example, As in SG-0_{aq} was 36.74 ppm, nearly 100 times higher than that of SG-1_{aq}, while Fe in SG-0_{aq} (518.88 ppm) was ~ 27 times higher than that of SG-1_{aq} and ~ 320 times higher than that of SG-2_{aq}- ~ SG-7_{aq} (1.60 ppm on average). For Au, the concentration in SG-1_{aq} was ~ 9 times higher than that of the rest samples. It is commonly understood that pyrite (a sulfide mineral) can be easily oxidized in aerobic or moist

Table 1 Fe, As and Au contents in the acid etching solution (SG-N_{aq}) and the etched pyrite surface layer (SG-N_s) respectively

Solution samples	$Fe_{(aq)}$ (ppm)	$As_{(aq)}$ (ppm)	$Au_{(aq)}$ ($\times 10^{-1}$ ppm)	Surface samples	$As_{(s)}$ (at.%)	$Au_{(s)}$ (at.%)	Etched depth (nm)
SG-0_{aq}	518.88 ± 24.74	36.74 ± 1.47	2.36 ± 0.40	SG-0_s	1.76 ± 0.04	0.0043 ± 0.0009	416.4
SG-1_{aq}	19.03 ± 0.94	0.31 ± 0.01	0.29 ± 0.08	SG-1_s	0.41 ± 0.03	0.014 ± 0.005	15.4
SG-2_{aq}	2.44 ± 0.12	0.18 ± 0.02	0.24 ± 0.05	SG-2_s	1.80 ± 0.33	0.09 ± 0.02	2.0
SG-3_{aq}	2.02 ± 0.07	0.15 ± 0.01	0.23 ± 0.03	SG-3_s	1.87 ± 0.08	0.11 ± 0.01	1.7
SG-4_{aq}	1.63 ± 0.02	0.13 ± 0.01	0.29 ± 0.03	SG-4_s	2.05 ± 0.11	0.17 ± 0.02	1.3
SG-5_{aq}	1.25 ± 0.07	0.11 ± 0.01	0.19 ± 0.07	SG-5_s	2.17 ± 0.19	0.14 ± 0.05	1.1
S6-6_{aq}	1.46 ± 0.19	0.11 ± 0.01	0.23 ± 0.04	S6-6_s	1.99 ± 0.17	0.15 ± 0.03	1.2
SG-7_{aq}	1.43 ± 0.17	0.10 ± 0.03	0.43 ± 0.14	SG-7_s	1.67 ± 0.30	0.29 ± 0.13	1.1

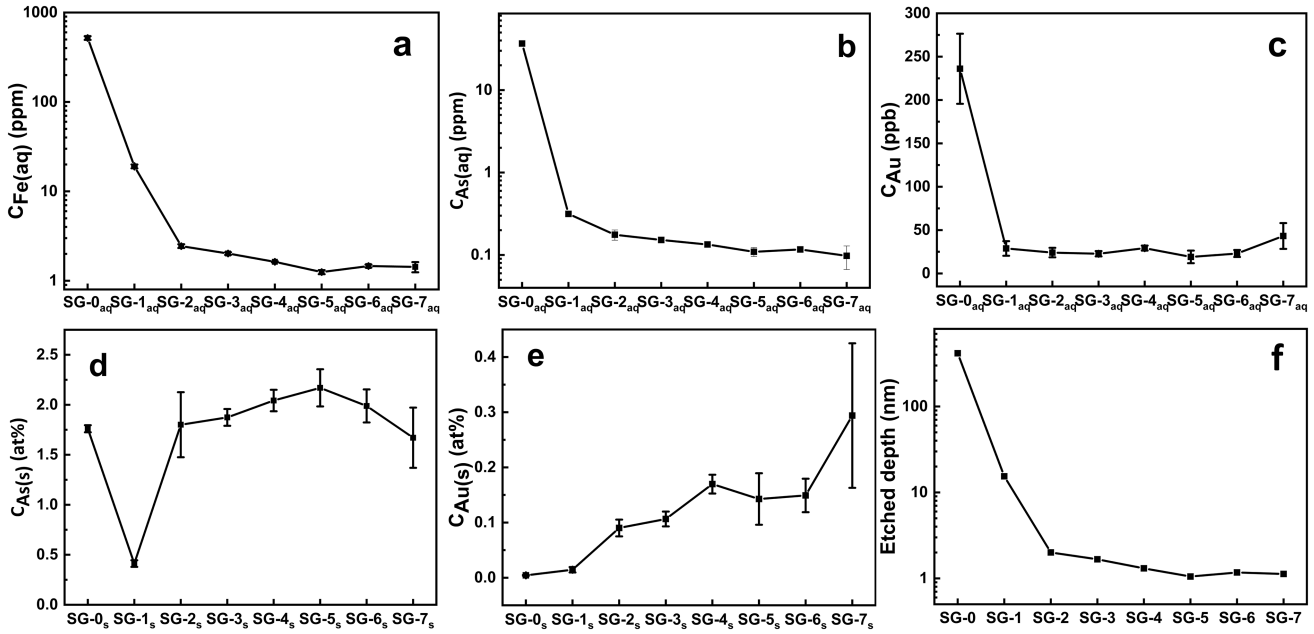

Fig. 2 Fe (**a**), As (**b**), and Au (**c**) concentrations in acid etching solutions SG-N_{aq} (N = 0–7) from powder samples SG-N (N = 0–7), estimated contents of As (**d**) and Au (**e**) in etched pyrite layer SG-N_s (N = 0–7), and approximate etched depth in each step (**f**)

environment, and the oxidation product such as $Fe(OH)_3$ or SO_4^{2-} can be easily removed by an acid solution (Qiu et al. 2018; Zhu et al. 2018). Thus, the observation of the highest elemental contents at the first acid etching step is attributed to the existence of an oxidation layer on the outermost surface of pyrite, which is also confirmed in our XPS study (Sect. 3.4). We speculate that the ore powder SG-0 was most likely oxidized during the pretreatment and storage processes.

When normalized by the amount of each etched layer of pyrite (SG-N_s), the As and Au contents in terms of atomic percentages in the etched pyrite present a totally different variation pattern (as shown in Fig. 2d–e). The calculated percentages of As in SG-N_s were relatively stable in the range of 1.7–2.2 at.%, except in SG-2_s where it dramatically dropped to a minimum of $\sim$ 0.4 at.%. This "anomalous" minimal value is probably due to the higher oxidizing speed of As in comparison with that of Fe and S, and thus easier migration of As to pyrite surface (Schaufuss et al. 2000). Consequently, a certain amount of As originally in the surface of SG-1 might have migrated into SG-0, which was sufficient enough to make SG-1_s As-poor comparing with other layers. In contrast, the Au concentrations practically maintained a persistent rising trend with the increasing etched depths. It should be emphasized that the above phenomenon might have reflected the very important pattern of ore fluid evolution at the final stage of pyrite mineralization, when Au became depleted as a consequence of deposition on pyrite overgrowth but As still remained in adequate supply (Kusebauch et al. 2019).

The etched depths (Table 1) were derived from Eq. (2) based on the mass of dissolved pyrite, and essentially depended on the Fe and As contents in the etched solutions. Thus, it is straightforward to see that the etched depths (in SG-N_s) resemble the Fe and As contents (in SG-N_{aq}) in terms of their variation with increasing etching steps. For instance, the maximal dissolved amount of Fe from SG-0 corresponded to the thickest etched depth of $\sim$ 416 nm in SG-0_s. Then the etched depth of SG-1_s decreased to $\sim$ 15 nm, still much higher than the subsequent steady etched depths (< 2 nm), indicating perhaps considerable degrading of crystal structure in the surface of SG-1 due to oxidation. Noticeably, the stabilization of etched depths reaching $\sim$ 1 nm suggests that pyrite etching is controllable under well-defined acid etching condition. Furthermore, combined with other techniques, such a wet chemistry etching method is demonstrated to enable depth profiling of arsenian pyrite to obtain important analytical data (e.g., Table 1) at nanoscale resolution.

3.4 XPS analysis

XPS spectra of powder samples SG-N are presented in Fig. 3. The binding energies of Fe 2p, S 2p and As 3d in SG-0 all showed remarkable blue shift compared with other samples, signifying existence of an oxidized surface layer of pyrite in SG-0 (Moulder et al. 1992), which also complies with the oxidation-promoted dissolution discussed in Sect. 3.3. For unoxidized pyrite (SG-1–SG-7), Fe $2p_{3/2}$ binding energy located at $\sim$ 706.8 indicates the

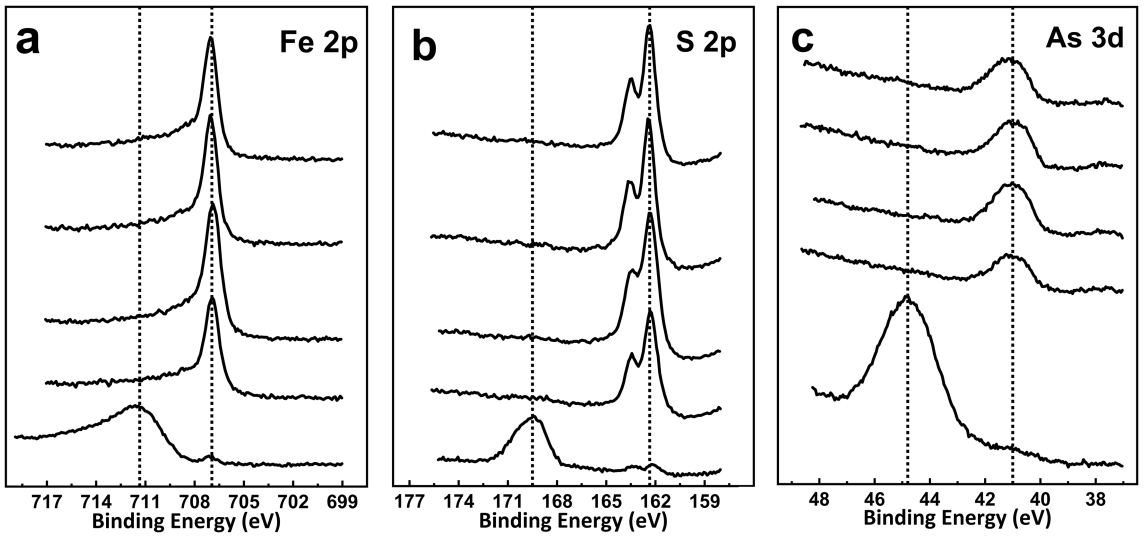

Fig. 3 Fe 2p (**a**), S 2p (**b**) and As 3d (**c**) XPS spectra of samples SG-N (N = 0–4, from bottom to top) respectively

reduced chemical state of FeS_2 (Binder 1973), while for SG-0, the major peak of Fe $2p_{3/2}$ at $\sim$ 711.2 eV suggests the oxidized form of Fe^{3+} and the much smaller peak at lower binding reveals a minor amount of unoxidized FeS_2 (Oku and Hirokawa1976). Similarly, the S 2p binding energy at 168.8 eV for SG-0 indicates the oxidized SO_4^{2-} species, and the smaller peak at 161.9 eV (same as that for SN-1–4) suggests minor unoxidized FeS_2 (Karthe et al. 1993; Volmeruebing and Stratmann 1992). The coexistence of both oxidized and unoxidized species in SG-0 may be due to partial detachment of the oxidation products from pyrite surface during milling and ultrasonication, which resulted in exposure of some detectable "fresh" pyrite. Again, As 3d peak in SG-0 at $\sim$ 44.8 eV verifies nearly complete oxidation to As^{3+} (Mizokawa et al. 1978). And the binding energies of As 3d in SG-1–4 were all at $\sim$ 41.0 eV corresponding to the valence state as As^{-} (Chanturiya et al. 2019; Liang et al. 2013), which is in accordance with the isovalent substitution of As for S in the pyrite lattice (Cook and Chryssoulis 1990; Reich et al. 2005), and also compatible with the negative correlation between As and S shown in Fig. 1f.

The Fe, S and As contents in samples SG-N (N = 0–4) were calculated by peak fitting of XPS spectra with CasaXPS software (Table 2). Sample SG-0 was found to have the highest atomic percentages of Fe and As, but the lowest S content among all tested samples. Such characteristic of the surface-oxidized sample SG-0 is most likely due to partial elution of some dissolvable oxidized S species (e.g., sulfate) during powder sample pretreatment (e.g., sonication, panning in water) combined with better preservation of the less dissolvable Fe and As oxidation products. The Fe, S and As contents in samples SG-1–4 all changed very little, inferring insignificant influence on the composition and structure of the deeper "clean" pyrite by our repeated acid etching procedure.

Table 2 Atomic percentages of Fe, S and As in samples SG-N (N = 0–4) based on XPS spectra fitting

	Fe (at.%)	S (at.%)	As (at.%)
SG-0	43.25 ± 4.87	48.03 ± 5.22	8.72 ± 0.44
SG-1	32.72 ± 2.17	65.30 ± 2.05	1.98 ± 0.12
SG-2	32.26 ± 1.14	65.82 ± 1.08	1.92 ± 0.07
SG-3	31.12 ± 2.20	66.83 ± 2.13	2.06 ± 0.07
SG-4	32.66 ± 0.06	65.31 ± 0.07	2.02 ± 0.03

Caution should be advised when a cross-comparison is attempted between the etching solutions (Sect. 3.3) and XPS analysis (Sect. 3.4) results, since disagreement seems to be inevitable (especially for the shallow oxidation-affected samples) because of not only the differences in the targeted samples (dissolved vs. solid surface), but also a mismatch in the detection depth between acid etching and XPS (normally $\sim$ 10 nm) (Benoit 2003).

3.5 Ion sputter etching

Since ion sputtering is a conventional technique to help analyze materials layer-by-layer (Hofmann 1991), we applied ion (Ar^+) beam sputtering on sample SG-4 in order to draw a comparison with our acid etching method. As clearly shown in Fig. 4, after Ar^+ sputtering for just 1 min, the Fe 2p, S 2p and As 3d peaks were dramatically broadened compared with the original spectra, while further accumulating the sputtering time to 2 min did not seem to cause additional apparent changes in peak shape.

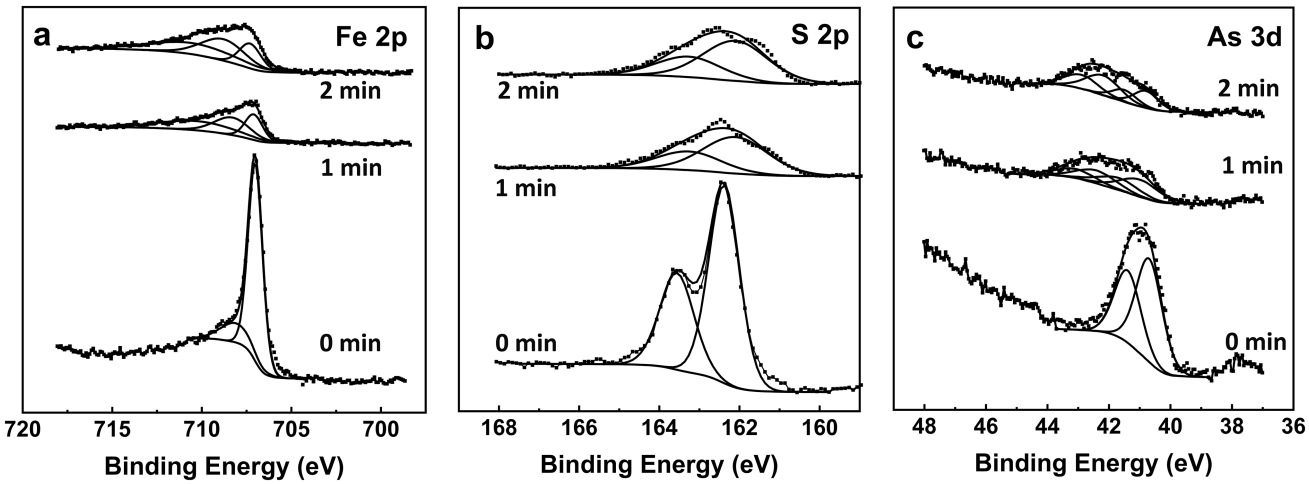

Fig. 4 Fe 2p (**a**), S 2p (**b**) and As 3d (**c**) XPS spectra of SG-4 after Ar^+ ion sputtering for 0, 1 and 2 min respectively

Meanwhile, after ion sputtering, the S 2p XPS spectra shifted to relatively lower binding energy, whereas the Fe 2p and As 3d XPS spectra shifted to higher binding energies (standing for more oxidized valence state). According to the peak fitting results (Table 3), ion sputtering for 2 min decreased the atomic percentage of S from 65.6% to 57.8%, and adversely increased Fe from 32.2% to 40.3%. This phenomenon can be attributed to the preferential sputtering of lighter element S in comparison with the relatively heavier elements Fe and As (Brijs et al. 1993; Koslowski et al. 2020). Nevertheless, in view of the severe sample damage due to Ar^+ ion sputtering as discussed above, our wet chemistry method, acid etching has demonstrated superior advantages in conducting depth profiling of pyrite samples.

3.6 Acid etching of synthetic pyrite

The ore samples in our acid etching experiments contain mixtures of minerals including pyrite with polydisperse size. Such non-uniformity in composition and size may add complication (e.g., necessity of reasonable assumptions) to the interpretation of the depth profiling data. We thus further test the acid etching method on synthetic single-component pyrite (P) and arsenian pyrite (AP $\sim$ 2.3 wt% As) samples, respectively. Samples were prepared following a previously reported synthetic method and were both cubic with a uniform size of $\sim$ 600 nm (luo et al. 2018). The Fe, As contents and the etched depths (shown in Fig. 5) all display roughly the same variation pattern with increasing etching steps as that of our natural ore samples from Carlin-type gold deposit, which features the highest elemental contents and etched depth at the first etching step due to oxidation, and then dramatically decreased and stabilized such values at the subsequent etching steps. The above consistence clearly corroborates the effectiveness and reproducibility of our acid etching method on ore samples as well as different types of mineral samples.

3.7 Extension of acid etching time

We have demonstrated depth profiling through non-oxidative acid etching with several advantages over many modern instrumental techniques, including negligible sample damage and nanoscale etching resolution. It is obviously desirable to gain further control on the etching process through manipulating the wet chemistry conditions (e.g., etchant composition, etching time). Here we tested whether etching steps could be conveniently enlarged by simply extending the etching time. As shown in Fig. 6, the dissolved Fe content kept raising almost linearly with increasing etching time from 90 to 360 min. Thus, it can be

Table 3 Fe $2p_{3/2}$, S $2p_{3/2}$ and As 3d binding energies and corresponding elemental contents of sample SG-4 after different duration of Ar^+ ion beam sputtering

Element	Cumulative etching time	0 min	1 min	2 min
Fe	Bind energy (eV)	706.9, 708.3	707.1, 708.3, 710.2	707.3, 708.8, 710.2
	Content (at.%)	32.2	34.7	40.3
S	Bind energy (eV)	162.2	162.1	162.1
	Content (at.%)	65.6	63.1	57.8
As	Bind energy (eV)	40.7	41, 42.4	40.8, 42.2
	Content (at.%)	2.2	2.2	2.0

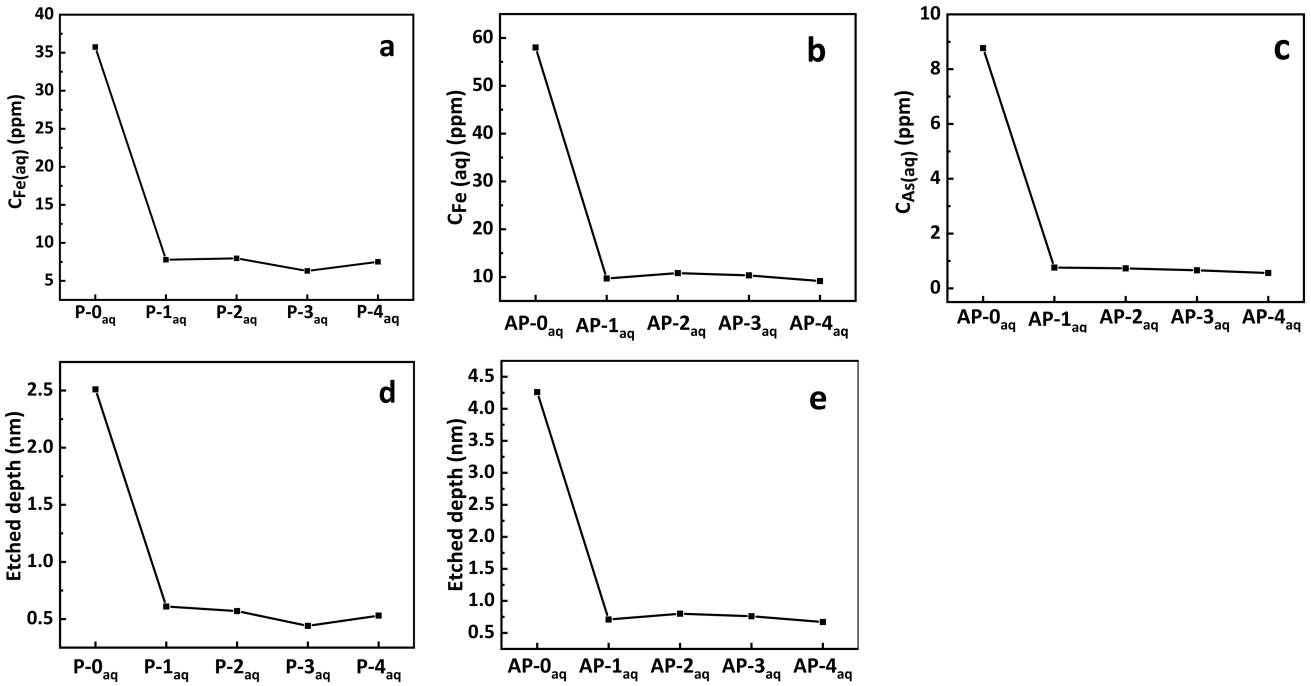

Fig. 5 Fe (**a**) concentrations in acid etching solutions P-N_{aq} (N = 0–4) from pyrite powder samples P-N (N = 0–4), Fe (**b**) and As (**c**) concentrations in acid etching solutions AP-N_{aq} (N = 0–4) from arsenian pyrite powder samples AP-N (N = 0–4), and approximate thicknesses of the etched pyrite P-N_s (**d**) and arsenian pyrite AP-N_s (**e**) layers, respectively

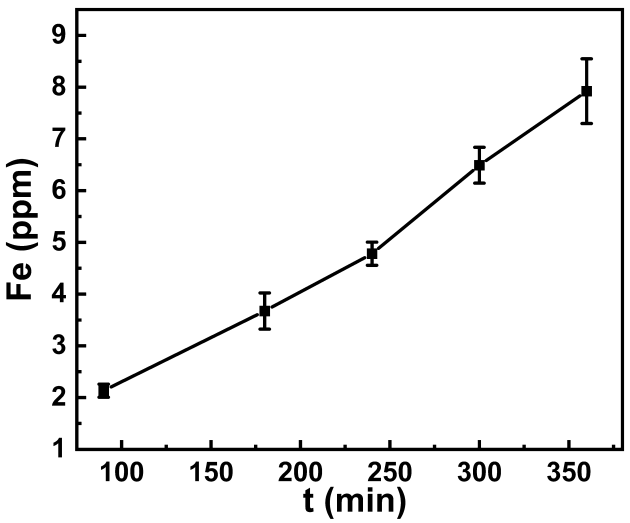

Fig. 6 Fe contents from samples SG-3 in acid etching solutions with increasing etching times

seen that the etched depth can be expanded not only by repeating etching cycles (e.g., from SG-0 to SG-7), but also by accumulating a single acid etching time (e.g., from 90 to 360 min). The above results also imply that the equilibrium of pyrite dissolution was far from being reached under our experimental conditions, which is also consistent with our calculation based on the solubility constant.

4 Conclusion

Depth profiling of arsenian pyrite was successfully conducted based on non-oxidizing acid etching combined with other analytical techniques. In contrast to conventional surface etching methods (such as ion beam etching) potentially suffering severe sample damage, our wet chemistry method is considered to cause insignificant alteration to the elemental composition and chemical state of the arsenian pyrite samples. The etched depth is directly estimated through the Fe and As contents in etching solutions (instead of through calibration), and can easily and reproducibly reach nanoscale resolution surpassing that of many modern characterization techniques. In addition, in comparison with ion sputtering toward one direction, wet chemistry etching on all facets of mineral grains is more isotropic and thus endows statistically enhanced sample representativeness. The high resolution As and Au depth profiles revealed in this study can provide critical new insights into the ore-forming process in Carlin-type gold deposit. We also expect expanded application of such wet chemistry methodology in additional areas of studies.

Acknowledgements Financial supports from the B-type Strategic Priority Program of the Chinese Academy of Sciences (Grant No. XDB41000000), the National Natural Science Foundation of China (41872046, 41902041 and 41173074) and the Natural Science Research Project of Education Department of Guizhou Province (No. KY[2018]004) are sincerely acknowledged. We also greatly

appreciate the assistances from Prof. Yong Xia (the Institute of Geochemistry, Chinese Academy of Sciences, China) for sample collection and Dr. Yuanyuan Cui (Shimadzu China Co. LTD) for XPS analysis, respectively.

Author contributions Conceptualization, QW; methodology, MY and QW; software, XN and WL; validation, XN and PZ; investigation, MY and XN; resources, SL and YF; data curation, MY and WL; formal analysis, SL and PZ; writing-original draft preparation, MY; writing-review and editing, QW; visualization, MY and YF; supervision, QW and SL; funding acquisition, QW; All authors have read and agreed to the published version of the manuscript.

Declarations

Conflict of interest All authors have no conflicts to declare.

References

Agangi A, Hofmann A, Wohlgemuth-Ueberwasser CC (2013) Zoning as a record of mineralization in the Ventersdorp Contact Reef, Witwatersrand Basin, South Africa. Econ Geol 108(6):1243–1272. https://doi.org/10.2113/econgeo.108.6.1243

Artyushkova K, Levendosky S, Atanassov P, Fulghum J (2007) XPS structural studies of nano-composite non-platinum electrocatalysts for polymer electrolyte fuel cells. Top Catal 46(3):263–275. https://doi.org/10.1007/s11244-007-9002-y

Barker SLL, Hickey KA, Cline JS, Dipple GM, Kilburn MR, Vaughan JR, Longo AA (2009) Uncloaking invisible gold: use of NanoSIMS to evaluate gold, trace elements, and sulfur isotopes in pyrite from Carlin-type gold deposits. Econ Geol 104(7):897–904. https://doi.org/10.2113/econgeo.104.7.897

Benoit R (2003) X-ray photoelectron spectroscopy. Vide Sci Tech Appl 58(308):219

Binder H (1973) Investigations on nature of chemical bonds in iron-sulfur compounds using X-ray photoelectron spectroscopy. Z Naturforsch B 28(5–6):255–262. https://doi.org/10.1515/znb-1973-5-607

Brijs B, Bender H, Decoster W, Moons R, Vandervorst W (1993) In-situ RBS analysis of ion-beam mixing during low-energy sputtering. Nucl Instrum Methods B 79(1–4):446–449. https://doi.org/10.1016/0168-583X(93)95384-H

Cepedal A, Fuertes-Fuente M, Martin-Izard A, Gonzalez-Nistal S, Barrero M (2008) Gold-bearing As-rich pyrite and arsenopyrite from the El Valle gold deposit, Asturias, northwestern Spain. Can Mineral 46:233–247. https://doi.org/10.3749/canmin.46.1.233

Chanturiya V, Bunin I, Ryazantseva M (2019) XPS study of sulfide minerals surface oxidation under high-voltage nanosecond pulses. Miner Eng. https://doi.org/10.1016/j.mineng.2019.105939

Cook NJ, Chryssoulis SL (1990) Concentrations of invisible gold in the common sulfides. Can Mineral 28:1–16

Deditius AP, Reich M, Kesler SE, Utsunomiya S, Chryssoulis SL, Walshe J, Ewing RC (2014) The coupled geochemistry of Au and As in pyrite from hydrothermal ore deposits. Geochim Cosmochim Acta 140:644–670. https://doi.org/10.1016/j.gca.2014.05.045

Della LD, Mueller W, Rasmussen SO, Svensson A, Vallelonga P (2017) Calibrated cryo-cell UV-LA-ICPMS elemental concentrations from the NGRIP ice core reveal abrupt, sub-annual variability in dust across the GI-21.2 interstadial period. CRYOSPHERE 11(3):1297–1309. https://doi.org/10.5194/tc-11-1297-2017

Dowsett M, Adriaens A (2004) Role of SIMS in cultural heritage studies. Nucl Instrum Methods B 226(1–2):38–52. https://doi.org/10.1016/j.nimb.2003.12.086

Fleet ME, Mumin AH (1997) Gold-bearing arsenian pyrite and marcasite and arsenopyrite from Carlin Trend gold deposits and laboratory synthesis. Am Mineral 82(1–2):182–193. https://doi.org/10.2138/am-1997-1-220

Gopon P, Douglas JO, Auger MA, Hansen L, Wade J, Cline JS, Robb LJ, Moody MP (2019) A nanoscale investigation of Carlin-type gold deposits: an atom-scale elemental and isotopic perspective. Econ Geol 114(6):1123–1133. https://doi.org/10.5382/econgeo.4676

Hnatyshin D, Creaser RA, Meffre S, Stern RA, Wilkinson JJ, Turner EC (2020) Understanding the microscale spatial distribution and mineralogical residency of Re in pyrite: Examples from carbonate-hosted Zn-Pb ores and implications for pyrite Re-Os geochronology. Chem Geol. https://doi.org/10.1016/j.chemgeo.2019.119427

Hofmann S (1991) Compositional depth profiling by sputtering. Prog Surf Sci 36(1):35–87. https://doi.org/10.1016/0079-6816(91)90013-T

Hou L, Peng HJ, Ding J, Zhang JR, Zhu SB, Wu SY, Wu Y, Ouyang HG (2016) Textures and in situ chemical and isotopic analyses of pyrite, Huijiabao trend, Youjiang basin, China: Implications for paragenesis and source of sulfur. Econ Geol 111(2):331–353. https://doi.org/10.2113/econgeo.111.2.331

Hu K, Pan MC, Cao J, Liu Y, Han SC (2017) The Au-hosting minerals and process of formation of the Carlin-type Bojitian Deposit, Southwestern China. Geofluids. https://doi.org/10.1155/2017/2417209

Jl L, Li J, Liu XM, Zhai W, Huang Y, Ji Z, Sun WD, Song MC, Li JZ (2020) Multiple element mapping and in-situ S isotopes of Au-carrying pyrite of Shuiyindong gold deposit, southwestern China using NanoSIMS: Constraints on Au sources, ore fluids, and mineralization processes. Ore Geol Rev. https://doi.org/10.1016/j.oregeorev.2020.103576

Karthe S, Szargan R, Suoninen E (1993) Oxidation of pyrite surfaces-a photoelectron spectroscopic study. Appl Surf Sci 72(2):157–170. https://doi.org/10.1016/0169-4332(93)90007-X

Koslowski HR, Schmitz J, Linsmeier C (2020) Temporally resolved LEIS measurements of Cr segregation after preferential sputtering of WCrY alloy. Nucl Instrum Methods B 479:42–46. https://doi.org/10.1016/j.nimb.2020.06.005

Kusebauch C, Gleeson SA, Oelze M (2019) Coupled partitioning of Au and As into pyrite controls formation of giant Au deposits. Sci Adv. https://doi.org/10.1126/sciadv.aav5891

Large RR, Danyushevsky L, Hollit C, Maslennikov V, Meffre S, Gilbert S, Bull S, Scott R, Emsbo P, Thomas H, Singh B, Foster J (2009) Gold and trace element zonation in pyrite using a laser imaging technique: implications for the timing of gold in Orogenic and Carlin-style sediment-hosted deposits. Econ Geol 104(5):635–668. https://doi.org/10.2113/gsecongeo.104.5.635

Li JX, Hu RZ, Zhao CH, Z JJ, H Y, G W, Li JW, Z YZ, (2020) Sulfur isotope and trace element compositions of pyrite determined by NanoSIMS and LA-ICP-MS: new constraints on the genesis of the Shuiyindong Carlin-like gold deposit in SW China. Miner Depos 55(7):1279–1298. https://doi.org/10.1007/s00126-019-00929-w

Liang JL, Sun WD, Li YL, Zhu SY, Li H, Liu YL, Zhai W (2013) An XPS study on the valence states of arsenic in arsenian pyrite: Implications for Au deposition mechanism of the Yang-shan Carlin-type gold deposit, western Qinling belt. J Asian Earth Sci 62:363–372. https://doi.org/10.1016/j.jseaes.2012.10.020

Luo SX, Nie X, Yang MZ, Fu YH, Zeng P, Wan Q (2018) Sorption of differently charged gold nanoparticles on synthetic pyrite. Minerals. https://doi.org/10.3390/min8100428

Mao SH (1991) Occurrence and distribution of invisible gold in a Carlin-type gold deposit in China. Am Mineral 76(11–12):1964–1972

Mikhlin YL, Romanchenko AS (2007) Gold deposition on pyrite and the common sulfide minerals: An STM/STS and SR-XPS study of surface reactions and Au nanoparticles. Geochim Cosmochim Acta 71(24):5985–6001. https://doi.org/10.1016/j.gca.2007.10.001

Mizokawa Y, Iwasaki H, Nishitani R, Nakamura S (1978) ESCA studies oF Ga, As, GaAs, Ga_2O_3, As_2O_3 and As_2O_5. J Electron Spectrosc Relat Phenom 14(2):129–141. https://doi.org/10.1016/0368-2048(78)85061-0

Moller P, Kersten G (1994) Electrochemical accumulation of visible gold on pyrite and arsenopyrite surfaces. Miner Depos 29(5):404–413. https://doi.org/10.1007/bf01886958

Moulder JF, Stickle WF, Sobol WM, Bomben KD (1992) Handbook of X-ray photoelectron spectroscopy. Perkin-Elmer Corporation

Muntean JL, Cline JS, Simon AC, Longo AA (2011) Magmatic-hydrothermal origin of Nevada's Carlin-type gold deposits. Nat Geosci 4(2):122–127. https://doi.org/10.1038/NGEO1064

Nobuta T, Ogawa T (2009) Depth profile XPS analysis of polymeric materials by C-60 (+) ion sputtering. J Mater Sci 44(7):1800–1812. https://doi.org/10.1007/s10853-009-3274-5

Oku M, Hirokawa K (1976) X-ray photoelectron-spectroscopy of Co_3O_4, Fe_3O_4, Mn_3O_4 and related compounds. J Electron Spectr Relat Phenom 8(6):475–481. https://doi.org/10.1016/0368-2048(76)80034-5

Palenik CS, Utsunomiya S, Reich M, Kesler SE, Wang LM, Ewing RC (2004) "Invisible" gold revealed: Direct imaging of gold nanoparticles in a Carlin-type deposit. Am Mineral 89(10):1359–1366. https://doi.org/10.2138/am-2004-1002

Qiu GH, TiY G, Hong J, Luo Y, Liu LH, Tan WF, Liu F (2018) Mechanisms of interaction between arsenian pyrite and aqueous arsenite under anoxic and oxic conditions. Geochim Cosmochim Acta 228:205–219. https://doi.org/10.1016/j.gca.2018.02.051

Reich M, Kesler SE, Utsunomiya S, Palenik CS, Chryssoulis SL, Ewing RC (2005) Solubility of gold in arsenian pyrite. Geochim Cosmochim Acta 69(11):2781–2796. https://doi.org/10.1016/j.gca.2005.01.011

Reich M, Deditius A, Chryssoulis S, Li JW, Ma CQ, Parada MA, Barra F, Mittermayr F (2013) Pyrite as a record of hydrothermal fluid evolution in a porphyry copper system: a SIMS/EMPA trace element study. Geochim Cosmochim Acta 104:42–62. https://doi.org/10.1016/j.gca.2012.11.006

Schaufuss AG, Nesbitt HW, Scaini MJ, Hoechst H, Bancroft MG, Szargan R (2000) Reactivity of surface sites on fractured arsenopyrite (FeAsS) toward oxygen. Am Mineral 85(11–12):1754–1766. https://doi.org/10.2138/am-2000-11-1219

Simon G, Huang H, Penner-Hahn JE, Kesler SE, Kao LS (1999a) Oxidation state of gold and arsenic in gold-bearing arsenian pyrite. Am Mineral 84(7–8):1071–1079. https://doi.org/10.2138/am-1999-7-809

Simon G, Kesler SE, Chryssoulis S (1999b) Geochemistry and textures of gold-bearing arsenian pyrite, Twin Creeks, Nevada: Implications for deposition of gold in Carlin-type deposits. Econ Geol 94(3):405–421. https://doi.org/10.2113/gsecongeo.94.3.405

Su WC, Xia B, Zhang HT, Zhang XC, Hu RZ (2008) Visible gold in arsenian pyrite at the Shuiyindong Carlin-type gold deposit, Guizhou, China: implications for the environment and processes of ore formation. Ore Geol Rev 33(3–4):667–679. https://doi.org/10.1016/j.oregeorev.2007.10.002

Su WC, Zhang HT, Hu RuZ, Ge X, Xia B, Chen YY, Zhu C (2012) Mineralogy and geochemistry of gold-bearing arsenian pyrite from the Shuiyindong Carlin-type gold deposit, Guizhou, China: implications for gold depositional processes. Miner Depos 47(6):653–662. https://doi.org/10.1007/s00126-011-0328-9

Su WC, Dong WD, Zhang XC, Shen NP, Hu RZ, Hofstra H, Cheng LZ, Xia Y, Yang KY (2018) Carlin-type gold deposits in the Dian-Qian-Gui "golden triangle" of Southwest China. In: Diversity of Carlin-style gold deposits. Soc Econ Geologists, Littleton, 157–185

Volmeruebing M, Stratmann M (1992) A surface analytical and an electrochemical study of iron surfaces modified by thiols. Appl Surf Sci 55(1):19–35. https://doi.org/10.1016/0169-4332(92)90377-A

Wang L, Zhu YF (2015) Multi-stage pyrite and hydrothermal mineral assemblage of the Hatu gold district (west Junggar, Xinjiang, NW China): implications for metallogenic evolution. Ore Geol Rev 69:243–267. https://doi.org/10.1016/j.oregeorev.2015.02.021

Wang JY, Starke U, Mittemeijer EJ (2009) Evaluation of the depth resolutions of Auger electron spectroscopic, X-ray photoelectron spectroscopic and time-of-flight secondary-ion mass spectrometric sputter depth profiling techniques. Thin Solid Films 517(11):3402–3407. https://doi.org/10.1016/j.tsf.2009.01.007

Yamaguchi T, Ishiyama T, Kishimoto H, Develos-Bagarinao K, Yamaji K (2020) Quantitative analysis of proton solubility in YSZ using SIMS. Solid State Ion. https://doi.org/10.1016/j.ssi.2020.115414

Yan J, Hu RZ, Liu S, Lin YT, Zhang JC, Fu SL (2018) NanoSIMS element mapping and sulfur isotope analysis of Au-bearing pyrite from Lannigou Carlin-type Au deposit in SW China: New insights into the origin and evolution of Au-bearing fluids. Ore Geol Rev 92:29–41. https://doi.org/10.1016/j.oregeorev.2017.10.015

Zhang XC, Spiro B, Halls C, Stanley CJ, Yang KY (2003) Sediment-hosted disseminated gold deposits in Southwest Guizhou, PRC: Their geological setting and origin in relation to mineralogical, fluid inclusion, and stable-isotope characteristics. Int Geol Rev 45(5):407–470. https://doi.org/10.2747/0020-6814.45.5.407

Zhang Y, Xia Y, Su WC, Tao Y, Zhang XC, Liu JZ, Deng YM (2010) Metallogenic model and prognosis of the Shuiyindong super-large strata-bound Carlin-type gold deposit, southwestern Guizhou Province, China. Chin J Geochem 29(2):157–166. https://doi.org/10.1007/s11631-010-0157-z

Zhao J, Liang JH, Long XP, Li J, Xiang QR, Zhang JC, Hao JL (2018) Genesis and evolution of framboidal pyrite and its implications for the ore-forming process of Carlin-style gold deposits, southwestern China. Ore Geol Rev 102:426–436. https://doi.org/10.1016/j.oregeorev.2018.09.022

Zheng LL, Yang RD, Gao JB, Chen J, Liu JZ, He YN (2016) Geochemical characteristics of the giant Nibao Carlin-type gold deposit (Guizhou, China) and their geological implications. Arab J Geosci 9(2):16. https://doi.org/10.1007/s12517-015-2077-z

Zhu JX, Xian HY, Lin XJ, Tang HM, Du RX, Yang YP, Zhu RL, Liang XL, Wei JM, Teng HH, He HP (2018) Surface structure-dependent pyrite oxidation in relatively dry and moist air: Implications for the reaction mechanism and sulfur evolution. Geochim Cosmochim Acta 228:259–274. https://doi.org/10.1016/j.gca.2018.02.050